# Suppression of crosstalk in coding CDWL by active FOV modulation with a deformable mirror

YUNBIN WU,[1] YUNPENG ZHANG,[1] JINLONG YUAN,[1,2] ZHIFENG SHU,[2] JINGJING DONG,[2] MANYI LI,[1] LIJIE ZHAO,[1] AND HAIYUN XIA[1,2,3,4,*]

[1] *School of Earth and Space Science, University of Science and Technology of China, Hefei, 230026, China*
[2] *School of Atmospheric Physics, Nanjing University of Information Science and Technology, Nanjing 210044, China*
[3] *Institute of Software, Chinese Academy of Sciences, Beijing 100190, China*
[4] *National Laboratory for Physical Sciences at the Microscale, University of Science and Technology of China, Hefei 230026, China*
*[*]hsia@ustc.edu.cn*

**Abstract:** Coding technology provides new ideas for spatial resolution enhancement of coherent Doppler wind lidar (CDWL). To improve the performance of coding CDWL for ultra-fine-wind field detection, the crosstalk between neighboring laser pulses is analyzed in theory. The strong backscattered signal from aerosols in near field region will interfere with the weak atmospheric signal, making the accuracy of Doppler shift estimation deteriorate seriously. Considering the formation mechanism of crosstalk, a solution based on adaptive field of view (FOV) modulation is proposed to suppress the crosstalk which is validated by numerical simulation and experiment. Dynamic range of the backscatter intensity is controlled from 10 dB to 2 dB within the distance of 50 m to 300 m, thus the crosstalk is accordingly suppressed.

## 1. Introduction

CDWL technology is developing rapidly. Benefitting from its compact structure, high spatial and temporal resolution, high measurement accuracy, long detecting range and strong anti-jamming ability, the CDWL has been applied in many fields, including air pollution monitoring [1–3], weather forecast [4–6], wind power generation [7–9], boundary layer evolution [10–12], and other scientific researches [13–17].

In many specific applications, such as wind tunnel, aircraft wake, and aerodynamics, remote sensing of small-scale flow structure is highly required. In these occasions, capability to detect the refined dynamic structure of wake vortices and turbulence in scale of below 10 meters is essential [18–22]. The highest spatial resolution of a commercial CDWL now is 15 m [23], which is still not sufficient for such detection tasks. The main factor limiting the further development of spatial resolution of all-fiber CDWL system is the single laser pulse energy. The spatial resolution of a lidar is approximately proportional to the full width at half-maximum (FWHM) of the transmitted laser pulse [24]. For higher spatial resolution of CDWL, laser with shorter duration is required. However, maintaining a required Carrier to noise ratio (CNR) to guarantee the accuracy of Doppler estimation, a laser with shorter pulse duration needs higher peak power, which is limited by the nonlinear optical phenomena, particularly the stimulated Brillouin scattering (SBS) in the fiber [25–28]. As a matter of fact, the same situation is also faced in optical fiber sensing. By modulating the emitted laser with appropriate coding scheme, the spatial resolution can be enhanced while maintaining a relatively high CNR. Therefore, pulse coding technology has been widely applied in distributed fiber sensors [29–34]. Meanwhile, the coding technology can be adopted in CDWL system to achieve meter-scale spatial resolution [35].

As to the CDWL, the pulse coding technique has its unique advantages. Firstly, it can raise the average transmitting power with limited peak power to improve the carrier-to-noise ratio (CNR). Secondly, compared to conventional CDWL with low pulse repetition frequency, the pulse coding technology offers higher retrieval accuracy by increasing the accumulation number of pulses at the same temporal resolution. Thirdly, the noise exposure time can be reduced as the coding CDWL can employ pulses with shorter duration. Meanwhile, CDWL using coding technology has a higher CNR with limited laser power, compared to other methods to improve the spatial resolution [36,37].

In the previous work [35], a problem limiting the performance of coding CDWL is found. Different from that in an optical fiber where the optical signal attenuation is relatively weak along the distance, the atmosphere has stronger attenuation which can cause a large gap of intensity between backscattered signals from different distances. Therefore, when the decoding operation is performed in frequency domain, the signal with large intensity will bring serious crosstalk to other weak signals. To solve this problem, a new scheme with deformable mirror (DM) is proposed. By modulating the field of view (FOV) of receiving telescope adaptively with the DM, flat backscattered signal can be obtained and the crosstalk can be suppressed.

In this work, the crosstalk in coding CDWL is firstly proposed and the theoretical analysis and simulation are carried out. Moreover, a solution to suppress the crosstalk by modulating the FOV adaptively with the DM is proposed and experimentally demonstrated. In the experiment section, the new scheme of coding CDWL with adaptive FOV modulation (FOVm) is validated.

## 2. Instrument

The setup of the new scheme for improve the performance of coding CDWL system is shown in Fig. 1. The scheme has two working modes: noncoding CDWL and coding CDWL. The working modes can be controlled by electrical pulse type generated by an arbitrary waveform generator (AWG). The noncoding CDWL working mode is mainly used for the adaptive FOVm algorithm which is described in Section 4. The improved coding CDWL layout is introduced here.
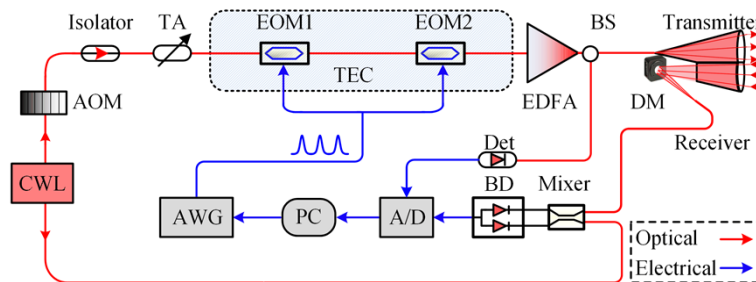


**Fig. 1.** Optical layout of the improved coding CDWL. CWL, continuous-wave laser; AOM, acoustic-optic modulator; TA, tunable attenuator; EOM, electro-optic modulator; TEC, thermo electric cooler; EDFA, erbium-doped fiber amplifier; BS, beam splitter; DM, deformable mirror; Det, detector; BD, balanced detector; A/D, analog-to-digital converter; AWG, arbitrary waveform generator; PC, personal computer.

The light emitted from a continuous-wave laser (CWL) is 80 MHz frequency-shifted by an acoustic-optic modulator (AOM) and chopped into coding pulse sequence by two electro-optic modulators (EOM) driven by electrical Golay code. Here, two EOMs settled in a thermostat are used to achieve a higher extinction ratio. After amplified by the erbium-doped fiber amplifier (EDFA), a small part of the coded laser is split out to an analog detector. Thus, the AWG can generate corrected electrical sequence signal to flatten the coded probing pulses [35]. Then, the probing pulses are transmitted to the atmosphere through a transmitter. On the other hand,

laser emitted from the local oscillator is mixed with the backscattered signal and collected by a balanced detector (BD). DM is used to flatten the backscattered signal. Finally, the mixed signal is converted to electrical signal by an analog-to-digital converter (A/D) and processed by a computer. The main parameters are listed in Table 1.

**Table 1. Key parameters of the improved coding CDWL**

| parameter | value |
|---|---|
| Wavelength (nm) | 1551 |
| Pulse energy (μJ) | 4.375 |
| Pulse duration (ns) | 40 |
| Pulse interval (ns) | 160 |
| Coding sequence interval(μs) | 12.52 |
| Diameter of collimator (mm) | 100 |
| Diameter of coupler (mm) | 80 |
| Sample rate (MS/s) | 500 |
| Aperture of DM (mm) | 10 |
| Response time of DM (ms) | 0.5 |
| Reflectance of DM (%) | 97.5 |

## 3. Principle and simulation

Golay code is a widely used complementary code, where the sum of the autocorrelations of all the codewords can expressed as:

$$A_k \otimes A_k + B_k \otimes B_k = 2L\delta_k, \tag{1}$$

where $\otimes$ is the operator of autocorrelation, $\delta_k$ is the delta function, $A_k$ and $B_k$ are the code elements ($\pm 1$), $L$ is the length of the coded sequences. For simplicity, we define an equivalent representation of the Eq.n. (1) as:

$$p_k \otimes p_k = 2L\delta_k, \tag{2}$$

where $p_k$ is the equivalent represent of the code elements. In lidar applications, only a unipolar optical pulse can be used. The bipolar Golay code sequence can be transformed to unipolar optical pulses with a simple linear transform [35].

Assuming the wind field is uniform in a short time, the following equations can be obtained:

$$STFT\{h(t)\} = \mathbf{H}(f, t) = H(f, t)e^{i\varphi(f, t)},$$
$$PSD\{h(t)\} = \mathbf{H}(f, t)\mathbf{H}^*(f, t) = H^2(f, t). \tag{3}$$

where $STFT\{\cdot\}$ and $PSD\{\cdot\}$ represent the spectrum of the signal via the short-time Fourier transform and its power spectral density, respectively. $h(t)$ is the backscattered signal of a single pulse, $H(f, t)$ and $\varphi(f, t)$ correspond to its amplitude and phase (the bold font represents the plural form), "*" is the conjugation operator.

In the following content, the label $(f, t)$ is omitted for the convenience of readers. Now the spectrum of one single pulse can be expressed as:

$$STFT\{h_k(t)\} = \mathbf{H}_k = He^{i\varphi_k}, \tag{4}$$

where $H$ and $\varphi_k$ are the constant amplitude and random phase of the spectrum. Afterwards, the spectrum of the coding CDWL can be written as:

$$
\begin{aligned}
cSTFT\{r(t)\} &= \sum_{m=1}^{L} p_m STFT\{h_{m-1}(t-(m-1)T_p)\} \\
&= \sum_{m=1}^{L} p_m H(t-(m-1)T_p)e^{i\varphi_{m-1}},
\end{aligned}
\tag{5}
$$

where $r(t)$ is the backscattered signal of the whole system, $T_p$ is the pulse interval. $H(t-(m-1)T_p)$ is simplified as $H_{m-1}$. Then, the PSD of the coding CDWL can be described as:

$$
\begin{aligned}
cR(t) = PSD\{r(t)\} &= \left\{ \sum_{n=1}^{L} p_n H_{n-1} e^{i\varphi_{n-1}} \right\} \left\{ \sum_{m=1}^{L} p_m H_{m-1} e^{-i\varphi_{m-1}} \right\} \\
&= \sum_{m=1}^{L}\sum_{n=1}^{L} p_n p_m H_{n-1} H_{m-1} e^{i(\varphi_{n-1}-\varphi_{m-1})} \\
&= \sum_{n=1}^{L} p_n H^2{}_{n-1} + \sum_{m=1}^{L}\sum_{n\neq m} p_n p_m H_{n-1} H_{m-1} e^{i(\varphi_{n-1}-\varphi_{m-1})} \\
&= E[R(t)] + e(t),
\end{aligned}
\tag{6}
$$

where $E[R(t)]$ is the mathematical expectation of the PSD and $e(t)$ represents the crosstalk term before decoding. After multiple measurements and accumulation, the $R(t)$ may approach its expectation value as:

$$
E[R(t)] = \sum_{n=1}^{L} p_n H_{n-1}^2 = \sum_{n=1}^{L} p_n H^2(f, t-(n-1)T_p).
\tag{7}
$$

After the decoding process, decoded PSD can be expressed as:

$$
\begin{aligned}
X(t) &= \sum_{k=1}^{L} p_k E[R(t+(k-1)T_p)] + \sum_{k=1}^{L} p_k e(t+(k-1)T_p) \\
&= 2L \cdot H^2(f, t+0) + \sum_{k=1}^{L} p_k e(t+(k-1)T_p) \\
&= 2L \cdot H^2(f, t) + \Delta(t),
\end{aligned}
\tag{8}
$$

where the $\Delta(t)$ is the crosstalk term after decoding. It should be noted that the mathematical expression is simplified. The omitted operations of transformation from bipolar codes to unipolar codes and decoding process was mentioned in our previous work [35]. Due to the limited accumulation in actual measurements, the crosstalk term will deteriorate the retrieval accuracy of wind velocity seriously. It can be expressed as:

$$
\begin{aligned}
\Delta(t) &= \sum_{k=1}^{L} p_k e(t+(k-1)T_p) \\
&= \sum_{k=1}^{L}\sum_{m=1}^{L}\sum_{m\neq n} p_k p_n p_m \mathbf{H_m}(t-(m-k)T_p)\mathbf{H_n^*}(t-(n-k)T_p).
\end{aligned}
\tag{9}
$$

The strong backscattered signals from near-field aerosols have a negative impact on other weak backscattered signals which cannot be eliminated and ignored though suppressing the crosstalk

by accumulation. The longer the code length, the wider the range of crosstalk effects. Therefore, suppressing the near-field backscattered signal is vital to reach ideal performance of coding CDWL. To intuitively explain the influence of crosstalk, a simulation comparison of coding CDWL and improved coding CDWL with flat backscattered signal is shown in Fig. 2.
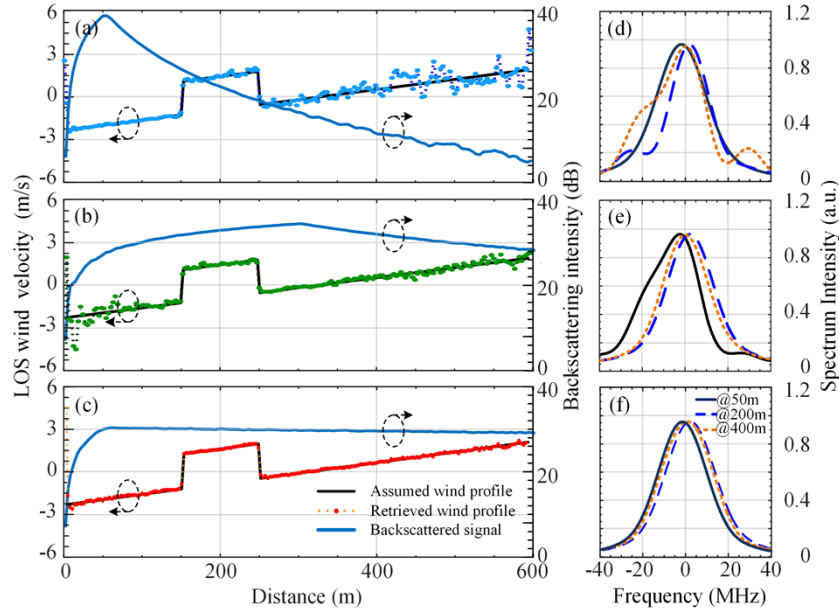


**Fig. 2.** (a), (b)and (c) are simulation results of coding CDWLs with different backscattering intensity curves, black tags with arrow indicate the corresponding Y-axis; (d), (e) and (f) are samples of normalized backscattering power spectrum density (PSD) of (a), (b) and (c).

In this simulation, a "feuillete" model [38] is used to simulate the backscattered signal of the atmosphere. Parameters of coding pulses are set as Table 1. White noise except shot noise is omitted here, so the fluctuation of retrieved wind velocity can directly represent the level of crosstalk. Figure 2 shows the simulation of three CDWLs based on Golay coding with different backscattered signal curves. The blue solid lines are normalized backscattered signal curves in logarithmic coordinates of the three cases with right axis. Figure 2(a) and (b) show coding CDWL that the backscattered signal are set to increase linearly to 50 m and 300 m, and then decay proportional to $z^2$ (where z means the distance away from telescope). Figure 2(c) shows the improved coding CDWL that the backscattered signal attenuate with relative flat profile at the distance between 50 m to 600 m. The black solid lines are assumed velocity profile. The blue, green and red dotted lines with circle are velocity derived from simulated backscattered signals of coding CDWL with left axis. Figure 2(b) shows a simple method to suppress the crosstalk which is shifting the full-overlap distance to far distance by just tilting transmitter and receiver. With full-overlap distance shifted from 50 m to 300 m, the crosstalk in far field is suppressed as intensity of near field backscattered signal decreasing. However, the crosstalk in near field gets harder, while improved coding CDWL with DM can avoid this problem. As shown in Fig. 2(c), the red velocity profile fits better with black assumed velocity profile.

Figure 2(d), (e) and (f) are samples of normalized PSD at different distance of three scheme. For comparison, they are normalized by the peak value. Without the influence of most noise, the distortion of PSD can be considered as mainly resulted from the crosstalk. Figure 2(d) shows that the PSD of coding CDWL becomes more and more distorted, as distance increases. Moreover, the distorted spectrum shows multi-peak structure due to serious crosstalk. While Fig. 2(e) shows

distorted spectrum in near field. As a comparison, PSD in Fig. 2(f) shows ideal single Gaussian structure with much less distortion. Therefore, flat backscattered signals can suppress crosstalk effectively.

## 4. Adaptive FOV modulation

Theoretically, the intensity of the backscattered signal of a CDWL rapidly attenuates as the distance increases due to the atmospheric extinction and the geometrical $1/z^2$ factor. Thus, the highest intensity of backscattered signal is obtained close to the telescope. However, the existence of geometrical compression suppresses the backscattered signal in near region, as the FOV of receiver and transmitter are not completely overlapped [39]. Generally, geometrical form factor is used to describe this influence in lidar field. As the distance increased, the signal compression becomes weaker, resulting in higher value of geometrical form factor. At the distance where all the backscattered signal is received, the factor equals to 1. The corresponding distance is called full-overlap distance where the intensity of backscattered signal is strongest.

FOVm can change the distribution of backscattered signal by adjusting the geometrical form factor. Appropriate FOVm with freeform optics can make geometrical form factor increase proportionally to $z^2$. Then, the backscattered signal attenuation with $1/z^2$ factor can be neutralized which leads to relatively flat backscattered signal [40]. In this work, Adaptive FOVm with DM is proposed that can both neutralize $1/z^2$ factor and eliminate the influence of atmospheric extinction, to obtain a flatter backscattered signal. The scheme with adaptive FOVm is shown in Fig. 1 and the workflow is shown in Fig. 3.
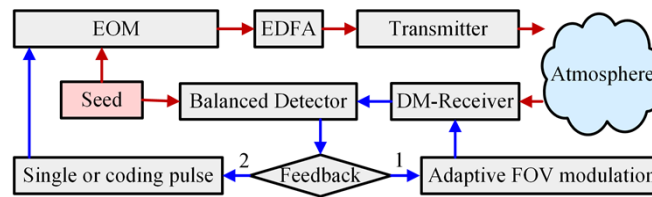


**Fig. 3.** Flow chart of the adaptive FOVm.

Firstly, the system starts as a single pulse electrical signal is transmitted to EOM. Then, the system is working in noncoding CDWL mode, where DM is used as an ordinary reflector. After the backscattered signal of noncoding CDWL is received, the real-time processed result of CNR is used as judgement condition of feedback loop. Adaptive FOVm (marked as 1 in Fig. 3) is realized through applying voltage to several segmented back electrodes glued to continuous reflective surface of DM. The feedback loop of adaptive FOVm ends until flat part of CNR is over 250 m. Then a sequence of coding pulses is sent to EOM (marked as 2 in Fig. 3) and the detection by coding CDWL starts. With adaptive FOVm method, the effects of atmosphere can be compensated, resulting in a flatter backscattered signal.

The DM is comprised of glass substrate with a reflective coating, which has a thin piezo ceramic disk with segmented electrodes glued to the back side. The inner mirror consisted with 40 segments has 3 connections to the bending arms, which in turn are fixed to the mirror supports. To demonstrated the capability of DM in FOVm, two red light at 632.8 nm lasers are directly connected to the telescope shown in Fig. 1. The results are shown in Fig. 4. The upper figures in Fig. 4(a)-(d) are faculae 3 m away from the telescope and the lower figures in Fig. 4(e)-(f) represent the corresponding voltage applied to the DM. The color bar shows the voltage span from 0 V to 200 V, corresponding to the physical strokes from 0 μm to 6.5 μm. Here, a flat mirror surface will appear at a control voltage level of 100 V. At voltages <100 V, the piezo material above the corresponding electrode will expand, leading to a local concave shape. While a voltage

>100 V, the piezo shrinks and leads to a local convex shape. Figure 4(a) shows the facula when DM is flat worked as an ordinary reflector, while Fig. 4(b)-(d) show facula patterns when inner mirror segments are applied with pre-defined voltage patterns.
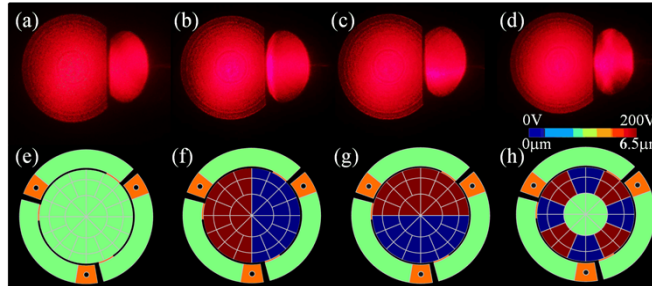


**Fig. 4.** Different facula patterns at 632.8 nm modulated by DM.

## 5.  Experiments and results

An improved coding CDWL with adaptive FOVm by DM is experimentally carried out to validate the new method. Meanwhile, a conventional noncoding CDWL is placed beside the system for comparison. The capability of conventional noncoding CDWL is shown in previous work [41–43]. The spatial resolutions of the coding CDWL and noncoding CDWL are 6 m and 30m, respectively. They share the same temporal resolution of 1 s. The length of Golay coding sequences is 128 and the repetition frequency of coding sequences is 5 kHz.

The results detected in different atmospheric conditions from March 11th and March 28th are plotted in Fig. 5 and Fig. 6, respectively. The comparison is carried out between conventional coding CDWL without adaptive FOVm and improved coding CDWL with adaptive FOVm. The blue solid lines stand for CNR. The dotted lines with circle in blue and orange represent the radial wind velocity of conventional coding CDWL and improved coding CDWL respectively.
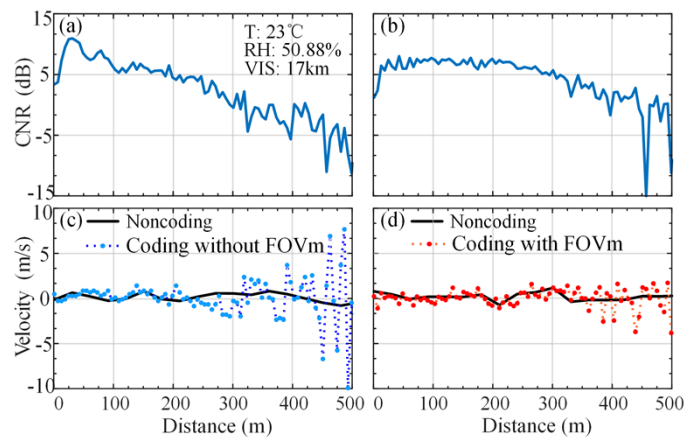


**Fig. 5.** (a) and (b) are CNR profiles of coding CDWL without adaptive FOVm and improved coding CDWL with adaptive FOVm detected on March 11th. (c) and (d) are corresponding radial wind velocity profiles

Figure 5(a) and Fig. 6(a) show CNR profiles with different slopes in different atmospheric conditions. With adaptive FOVm, backscattered signals are compensated to be flat between 50 m
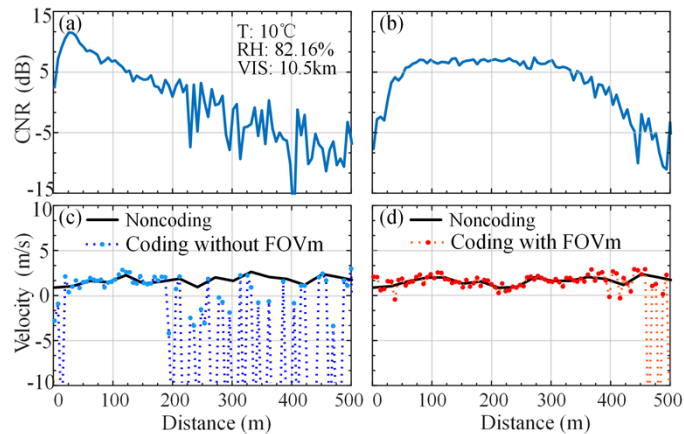
**Fig. 6.** (a) and (b) are CNR profiles of coding CDWL without adaptive FOVm and improved coding CDWL with adaptive FOVm detected on March 28th. (c) and (d) are corresponding radial wind velocity profiles

to 300 m in these two cases, due to a part of near-field energy is compensated to far field region. As a result, the maximum CNR of improved coding CDWL is about 5 dB lower than that of coding CDWL without FOVm. The length of flat region is related to several factors, including but not limited to divergence angle and aperture of telescope, adjustable range of piezo ceramics in DM and atmospheric conditions. Suffering from the crosstalk, CNR of coding CDWL without FOVm fluctuates substantially at distance over 200 m, and the accuracy of estimated wind velocity will become worse. While the radial wind velocity profiles of improved coding CDWL consist with the noncoding CDWL in wider range than those of coding CDWL without FOVm. These results imply that the improved coding CDWL has a better performance in different atmospheric conditions.

## 6. Conclusion

An improved coding CDWL applying adaptive FOVm technique is demonstrated by simulation and experiments. Through theoretical and simulation analysis, we found that the crosstalk in coding CDWL cannot be neglected, while the coding CDWL with flat backscattered signals can suppress crosstalk effectively. By comparing with normal coding CDWL without adaptive FOVm and noncoding CDWL in different atmospheric conditions, the new scheme is proved to be effective for suppressing the crosstalk and improving the accuracy and practicability of coding CDWL. It is worth mentioning that with the help of the DM, the received signal of the improved coding CDWL can be treated as 40 segments with different focal lengths. Then, the near-field backscattered signal is suppressed and far-field backscattered signal is enhanced. Thus the receiving efficiency changes to range dependent.

In general, the application of DM contributes to enhance the flexibility, variety and controllability of CDWL. In the future, we plan to apply DM with larger physical strokes and more tunable segments to further improve the performance of coding CDWL.

## References

1. Y. Yang, S. H. L. Yim, J. Haywood, M. Osborne, J. C. S. Chan, Z. Zeng, and J. C. H. Cheng, "Characteristics of Heavy Particulate Matter Pollution Events Over Hong Kong and Their Relationships With Vertical Wind Profiles Using High-Time-Resolution Doppler Lidar Measurements," J. Geophys. Res.: Atmos. **124**(16), 9609–9623 (2019).
2. J. Zhang, Z. Chen, Y. Lu, H. Gui, J. Liu, W. Liu, J. Wang, T. Yu, Y. Cheng, Y. Chen, B. Ge, Y. Fan, and X. Luo, "Characteristics of aerosol size distribution and vertical backscattering coefficient profile during 2014 APEC in Beijing," Atmos. Environ. **148**, 30–41 (2017).
3. T. Huang, Y. Li, J. C. H. Cheng, J. Haywood, K. K. Hon, D. H. Y. Lam, O. S. M. Lee, S. Lolli, E. J. O'Connor, and H. F. Lee, "Assessing Transboundary-Local Aerosols Interaction Over Complex Terrain Using a Doppler LiDAR Network," Geophys. Res. Lett. **48**(12), e2021GL093238 (2021).
4. N. J. Harvey, R. J. Hogan, and H. F. Dacre, "Evaluation of boundary-layer type in a weather forecast model utilizing long-term Doppler lidar observations," Q. J. R. Meteorol. Soc. **141**(689), 1345–1353 (2015).
5. W. E. Baker, G. D. Emmitt, F. Robertson, R. M. Atlas, J. E. Molinari, D. A. Bowdle, J. Paegle, R. M. Hardesty, R. T. Menzies, and T. N. Krishnamurti, "Lidar-measured winds from space: a key component for weather and climate prediction," Bull. Am. Meteorol. Soc. **76**(6), 869–888 (1995).
6. L. P. Thobois, R. Krishnamurthy, S. Loaec, J. P. Cariou, A. Dolfi-Bouteyre, and M. Valla, "Wind and EDR measurements with scanning Doppler LIDARs for preparing future weather dependent separation concepts," in *7th AIAA*, 3317 (2015).
7. G. Giebel, C. Draxl, R. Brownsword, G. Kariniotakis, and M. Denhard, "The state-of-the-art in short-term prediction of wind power. A literature overview," (2011).
8. T. Mikkelsen, "Lidar-based research and innovation at DTU wind energy–a review," in J. Phys., 012007 (2014).
9. D. A. Smith, M. Harris, A. S. Coffey, T. Mikkelsen, H. E. Jørgensen, J. Mann, and R. Danielian, "Wind lidar evaluation at the Danish wind test site in Høvsøre," Wind Energ. **9**, 87–93 (2006).
10. W. Diao, X. Zhang, J. Liu, X. Zhu, Y. Liu, D. Bi, and W. Chen, "All fiber pulsed coherent lidar development for wind profiles measurements in boundary layers," Chin. Opt. Lett. **12**(7), 072801 (2014).
11. X. Rui, P. Guo, H. Chen, S. Chen, Y. Zhang, M. Zhao, Y. Wu, and P. Zhao, "Portable coherent Doppler light detection and ranging for boundary-layer wind sensing," Opt. Eng. **58**(03), 1 (2019).
12. L. Wang, J. Yuan, H. Xia, L. Zhao, and Y. Wu, "Marine Mixed Layer Height Detection Using Ship-Borne Coherent Doppler Wind Lidar Based on Constant Turbulence Threshold," Remote Sens. **14**(3), 745 (2022).
13. T. Wei, H. Xia, K. Wu, Y. Yang, Q. Liu, and W. Ding, "Dark/bright band of a melting layer detected by coherent Doppler lidar and micro rain radar," Opt. Express **30**(3), 3654–3664 (2022).
14. T. Wei, H. Xia, B. Yue, Y. Wu, and Q. Liu, "Remote sensing of raindrop size distribution using the coherent Doppler lidar," Opt. Express **29**(11), 17246–17257 (2021).
15. B. Witschas, S. Rahm, A. Dörnbrack, J. Wagner, and M. Rapp, "Airborne Wind Lidar Measurements of Vertical and Horizontal Winds for the Investigation of Orographically Induced Gravity Waves," J. Atmos. Ocean. Technol. **34**(6), 1371–1386 (2017).
16. J. Yuan, K. Wu, T. Wei, L. Wang, Z. Shu, Y. Yang, and H. Xia, "Cloud Seeding Evidenced by Coherent Doppler Wind Lidar," Remote Sens. **13**(19), 3815 (2021).
17. M. Jia, J. Yuan, C. Wang, H. Xia, Y. Wu, L. Zhao, T. Wei, J. Wu, L. Wang, S.-Y. Gu, L. Liu, D. Lu, R. Chen, X. Xue, and X. Dou, "Long-lived high-frequency gravity waves in the atmospheric boundary layer: observations and simulations," Atmos. Chem. Phys. **19**(24), 15431–15446 (2019).
18. C. J. Oconnor and D. K. Rutishauser, "Enhanced airport capacity through safe, dynamic reductions in aircraft separation: NASA's Aircraft Vortex Spacing System (AVOSS)," (2001).
19. I. N. Smalikho and V. A. Banakh, "Estimation of aircraft wake vortex parameters from data measured with a 1.5-mum coherent Doppler lidar," Opt. Lett. **40**(14), 3408–3411 (2015).
20. S. Wu, X. Zhai, and B. Liu, "Aircraft wake vortex and turbulence measurement under near-ground effect using coherent Doppler lidar," Opt. Express **27**(2), 1142–1163 (2019).
21. H. Gao, J. Li, P. W. Chan, K. K. Hon, and X. Wang, "Parameter-retrieval of dry-air wake vortices with a scanning Doppler Lidar," Opt. Express **26**(13), 16377–16392 (2018).
22. I. N. Smalikho, V. A. Banakh, F. Holzäpfel, and S. Rahm, "Method of radial velocities for the estimation of aircraft wake vortex parameters from data measured by coherent Doppler lidar," Opt. Express **23**(19), A1194–A1207 (2015).
23. N. S. Prasad, R. Sibell, S. Vetorino, R. Higgins, and A. Tracy, "An all-fiber, modular, compact wind lidar for wind sensing and wake vortex applications," in International Society for Optics and Photonics, 94650C (2015).
24. D. T. Michel, A. Dolfi-Bouteyre, D. Goular, B. Augere, C. Planchat, D. Fleury, L. Lombard, M. Valla, and C. Besson, "Onboard wake vortex localization with a coherent 1.5 microm Doppler LIDAR for aircraft in formation flight configuration," Opt. Express **28**(10), 14374–14385 (2020).
25. H. A. Al-Asadi, M. H. Al-Mansoori, S. Hitam, M. I. Saripan, and M. A. Mahdi, "Particle swarm optimization on threshold exponential gain of stimulated Brillouin scattering in single mode fibers," Opt. Express **19**(3), 1842–1853 (2011).
26. R. G. Smith, "Optical power handling capacity of low loss optical fibers as determined by stimulated Raman and Brillouin scattering," Appl. Opt. **11**(11), 2489–2494 (1972).
27. C. Besson, A. Dolfi-Bouteyre, G. Canat, N. Cézard, B. Augère, A. Durecu, L. Lombard, M. Valla, and A. Hallermeyer, "Doppler LIDAR Developments for Aeronautics," Aerospace Lab, 1–16 (2016).

28. L. Lombard, M. Valla, C. Planchat, D. Goular, B. Augere, P. Bourdon, and G. Canat, "Eyesafe coherent detection wind lidar based on a beam-combined pulsed laser source," Opt. Lett. **40**(6), 1030–1033 (2015).

29. P. K. Sahu, S. C. Gowre, and S. Mahapatra, "Optical time-domain reflectometer performance improvement using complementary correlated Prometheus orthonormal sequence," IET Optoelectron. **2**(3), 128–133 (2008).

30. D. Lee, H. Yoon, P. Kim, J. Park, and N. Park, "Optimization of SNR improvement in the noncoherent OTDR based on simplex codes," J. Lightwave Technol. **24**(1), 322–328 (2006).

31. M. Nazarathy, S. A. Newton, R. P. Giffard, D. S. Moberly, F. Sischka, W. R. Trutna, and S. Foster, "Real-time long range complementary correlation optical time domain reflectometer," J. Lightwave Technol. **7**(1), 24–38 (1989).

32. M. D. Jones, "Using simplex codes to improve OTDR sensitivity," IEEE Photonics Technol. Lett. **5**(7), 822–824 (1993).

33. M. A. Soto, G. Bolognini, F. Di Pasquale, and L. Thévenaz, "Simplex-coded BOTDA fiber sensor with 1 m spatial resolution over a 50 km range," Opt. Lett. **35**(2), 259–261 (2010).

34. Y. Mao, N. Guo, K. L. Yu, H. Y. Tam, and C. Lu, "1-cm-Spatial-Resolution Brillouin Optical Time-Domain Analysis Based on Bright Pulse Brillouin Gain and Complementary Code," IEEE Photonics J. **4**(6), 2243–2248 (2012).

35. C. Wang, H. Xia, Y. Wu, J. Dong, T. Wei, L. Wang, and X. Dou, "Meter-scale spatial-resolution-coherent Doppler wind lidar based on Golay coding," Opt. Lett. **44**(2), 311–314 (2019).

36. Y. Zhang, Y. Wu, and H. Xia, "Spatial resolution enhancement of coherent Doppler wind lidar using differential correlation pair technique," Opt. Lett. **46**(22), 5550–5553 (2021).

37. Y. Zhang, Y. Wu, and H. Xia, "Spatial Resolution Enhancement of Coherent Doppler Lidar by Pseudo-Random Phase Coding," J. Lightwave Technol. **40**(13), 4467–4473 (2022).

38. P. Salamitou, A. Dabas, and P. H. Flamant, "Simulation in the time domain for heterodyne coherent laser radar," Appl. Opt. **34**(3), 499–506 (1995).

39. K. Stelmaszczyk, M. Dell'Aglio, S. Chudzyński, T. Stacewicz, and L. Wöste, "Analytical function for lidar geometrical compression form-factor calculations," Appl. Opt. **44**(7), 1323–1331 (2005).

40. J. Wojtanowski, "Cancelling lidar echo signal 1/range2 dependence and geometrical form factor shaping by the application of freeform optics," Opt. Laser Technol. **125**, 106011 (2020).

41. L. Wang, W. Qiang, H. Xia, T. Wei, J. Yuan, and P. Jiang, "Robust Solution for Boundary Layer Height Detections with Coherent Doppler Wind Lidar," Adv. Atmos. Sci. **38**(11), 1920–1928 (2021).

42. J. Yuan, L. Su, H. Xia, Y. Li, M. Zhang, G. Zhen, and J. Li, "Microburst, Windshear, Gust Front, and Vortex Detection in Mega Airport Using a Single Coherent Doppler Wind Lidar," Remote Sens. **14**(7), 1626 (2022).

43. J. Yuan, H. Xia, T. Wei, L. Wang, B. Yue, and Y. Wu, "Identifying cloud, precipitation, windshear, and turbulence by deep analysis of the power spectrum of coherent Doppler wind lidar," Opt. Express **28**(25), 37406–37418 (2020).